

# Degenerate type I nanosecond optical parametric oscillators

Arlee V. Smith, Darrell J. Armstrong, and Mark C. Phillips

*Department 1118, Lasers, Optics, and Remote Sensing, Sandia National Laboratories, Albuquerque, New Mexico 87185-1423*

Russell J. Gehr

*3000 Trinity Drive, Los Alamos, New Mexico 87544-2320*

Gunnar Arisholm

*Forsvarets Forskningsinstitutt (Norwegian Defence Research Establishment), P.O. Box 25, N-2027 Kjeller, Norway*

Received April 15, 2003; revised manuscript received July 7, 2003; accepted July 11, 2003

We present numerical modeling and laboratory studies of degenerate type I nanosecond optical parametric oscillators. Because the signal and idler waves are identical and parametric gain is phase sensitive, their round-trip phase is a critical parameter. We show that signal spectrum, transverse mode, and conversion efficiency are all strongly influenced by this phase. We also examine the influence of signal-wave injection seeding and phase-velocity mismatch. © 2003 Optical Society of America

*OCIS codes:* 190.4970, 190.4410, 190.2620.

## 1. INTRODUCTION

Degenerate optical parametric oscillators (OPO's) are of practical importance because they can be used as laser wavelength doublers that are useful in pumping infrared OPO's. Nonlinear crystals such as zinc germanium phosphide that are capable of reaching the 8–12- $\mu\text{m}$  range often absorb wavelengths shorter than 2  $\mu\text{m}$ , so wavelength doubling a Nd:YAG laser from 1064 to 2128 nm could provide a useful pump for infrared OPOs. If the wavelength doubling efficiency is greater than 0.5, and if the signal beam is of good quality and narrow linewidth, the 8–12- $\mu\text{m}$  power could be increased relative to 1064-nm pumping, even in the absence of 1064-nm absorption, because the number of 2128-nm photons would exceed the number of 1064-nm photons.

Another application of degenerate type I OPOs that is of current interest is in spatial and temporal pattern formation and amplification. In many recent theoretical studies<sup>1–4</sup> of cw, pump-resonant, degenerate OPO's it was discovered that, under certain conditions, interesting spatial and temporal patterns, including solitons, domain walls, and roll patterns, can form. These may have practical applications in information processing, but few careful experiments exploring these ideas in real laboratory devices have been performed. Our OPO is different from those OPOs in that it is neither cw nor pump resonant. Nevertheless, it exhibits some of the interesting spatial and temporal properties predicted, and it may serve to test further predictions, or it may have its own practical application in this field.

Type I degenerate OPOs are also used to generate nonclassical optical fields such as squeezed light.<sup>5–8</sup> Typically cw rather than pulsed OPOs are used in this appli-

cation as well, but our study of pulsed OPOs may illustrate some of the important factors that influence the performance of such devices.

OPOs are based on parametric mixing of three waves, the signal, the idler, and the pump, whose frequencies obey  $\omega_s + \omega_i = \omega_p$ . Depending on the relative phases of these three waves, energy can be transferred from the pump to the signal and the idler or from the signal and the idler to the pump. In the simplest OPO designs, only the signal wave is reflected by the OPO cavity mirrors. The pump and the idler make a single pass of the nonlinear crystal. At the input face of the crystal, the idler field's amplitude is zero, but as it propagates through the crystal it grows with the proper phase to maximize energy extraction from the pump. This is true regardless of the phase acquired by the signal wave on a round trip of the OPO cavity. One can continuously tune such singly resonant OPOs by adjusting the cavity's length and the crystal's phase-matched wavelength. Doubly resonant OPOs, which resonate both signal and idler, are more difficult to tune because the sum of the signal and the idler phases must have a certain value relative to the pump phase. Small changes in the length of the optical cavity can lead to spectral shifts of signal and idler to readjust these phases.<sup>9,10</sup> The required shift is inversely proportional to the difference in the group velocities of the signal and the idler waves in the nonlinear crystal. In a degenerate, type I OPO, the group-velocity difference is zero so the phase adjustment requires either large spectral shifts or some other accommodation such as beam tilts.

Signal and idler waves are indistinguishable in a collinear, degenerate type I OPO, so we combine them into a single wave that we call the signal. We consider only

OPOs that cause this signal but not the pump light to resonate. If we arbitrarily assign zero to the pump phase, a signal wave with a phase of either  $\pi/4$  or  $-3\pi/4$  will have maximum gain, whereas one with a phase of  $3\pi/4$  or  $-\pi/4$  will have maximum loss by means of frequency doubling or backconversion to pump light. If the OPO cavity is adjusted such that the round-trip signal phase is  $m\pi$ , where  $m$  is an integer, we expect that the OPO multipass gain will be maximized and the signal light will have one of the favored phases,  $\pi/4$  or  $3\pi/4$ . If  $m$  is an even integer, the signal field will be periodic, with a period equal to the cavity round-trip time. If  $m$  is an odd integer, the signal phase will change by  $\pi$  on each round trip, alternating between  $\pi/4$  and  $-3\pi/4$ , giving a period equal to two round trips; this corresponds to a shift of the longitudinal modes by half of the free spectral range of the OPO cavity relative to the modes with even  $m$ .

A broadband signal wave initiated from quantum vacuum might be expected to alternate more or less randomly between the two favored phases on a time scale much shorter than the cavity round-trip time, with the amplitude going to zero at the phase-switching points. The spatial counterpart of this pattern of constant-phase time domains separated by dark-domain boundaries is a spatial pattern of two-dimensional constant-phase domains separated by dark-line boundaries. It may also be possible under some circumstances to form linked spatial and temporal domain patterns.<sup>11</sup> The evolution and stability of these domains are expected to be determined by cavity-length detuning combined with signal dispersion in the case of time domains or combined with diffraction in the case of spatial domains. This notion motivated the theoretical studies of spatial pattern formation mentioned earlier.<sup>1-4</sup> If the spatial or temporal patterns were stable, they could be used to store and amplify digital information. Also note that the domain boundaries can have the essential features of dark solitons, namely, a dip in a uniform baseline irradiance, accompanied by a phase reversal. They might be a practical source of dark solitons for optical communication applications, for example.

If the phase of the pump fluctuates, as it does for broadband pump light, it is difficult to achieve proper phasing of the signal relative to the pump. The correct signal phase on one pass of the crystal will not necessarily be the correct phase on the next pass because the phase of the pump will have changed in an unpredictable way. Because of the instability of the pump phase, degenerate type I OPOs pumped by broad-bandwidth pump light can be expected to have high pump thresholds.

## 2. NUMERICAL MODELS

The nonlinear interaction and propagation of signal and pump waves are governed by two equations of the form<sup>12</sup>

$$\left( \frac{\partial}{\partial z} - \frac{i}{2k_j} \nabla_t^2 + \tan \rho_j \frac{\partial}{\partial x} + \frac{1}{v_j} \frac{\partial}{\partial t} + i\beta_j \frac{\partial^2}{\partial t^2} \right) \times \epsilon_j(x, y, z, t) = P_j(x, y, z, t) \exp(\pm i\Delta k z), \quad (1)$$

where the subscript  $j$  refers to either the signal or the pump wave,  $\nabla_t^2$  accounts for diffraction,  $\tan \rho_j$  describes birefringent walk-off with angle  $\rho_j$  in the  $x$  direction,  $v_j$  and  $\beta_j$  describe group velocity and group-velocity dispersion, respectively, and  $P_j$  is the driving polarization at frequency  $j$  that is due to the second-order nonlinearity of the crystal:

$$P_s = \frac{id_{\text{eff}}\omega_s}{cn_s} \epsilon_p \epsilon_s^*, \quad (2)$$

$$P_p = \frac{id_{\text{eff}}\omega_p}{cn_p} \epsilon_s \epsilon_s. \quad (3)$$

Phase mismatch  $\Delta k$  is defined as  $(k_p - 2k_s)$ , and the plus in the exponential term applies to the signal equation whereas the minus applies for the pump equation. The group velocity and group-velocity dispersion terms are defined, respectively, by

$$\frac{1}{v_j} = \left( \frac{dk_j}{d\omega} \right)_{\omega=\omega_j}, \quad (4)$$

$$\beta_j = -\frac{1}{2v_j^2} \left( \frac{dv_j}{d\omega} \right)_{\omega=\omega_j}. \quad (5)$$

$\epsilon(x, y, z, t)$  are envelope functions that modulate the pump and signal carrier waves of frequencies  $\omega_p$  and  $\omega_s = \omega_p/2$ , respectively. Most of our discussion will center on the effects of cavity-length variation when the crystal is tuned to exactly phase match degenerate mixing, so  $\Delta k$  is usually zero. We shall ignore linear absorption, nonlinear contributions to the refractive index, and multiphoton absorption.

The majority of our numerical studies used two models that separately address the temporal, or dispersive effects, and the spatial, or diffractive effects, of the OPO on the properties of the generated signal light. We shall see that often these two effects are important in different operating regimes, so using separate models is an efficient way to study them. We also sparingly used a numerical model of nanosecond OPO's that included both diffraction and dispersion<sup>12,13</sup> for those situations in which the spatial and temporal effects are likely to interact.

Temporal-spectral properties alone, including injection seeding, were handled by a modified version of our previously reported plane-wave, broad-bandwidth model that includes dispersive propagation,<sup>14</sup> whereas spatial effects alone were modeled by use of our monochromatic model that includes diffractive propagation.<sup>15</sup> The broad-bandwidth model is identical to what we called method 1 in an earlier paper,<sup>14</sup> except that we have modified method 1 to combine signal and idler waves into a single signal wave. The laboratory OPOs could be simulated with the plane-wave model without further approximations. However, because we needed many runs to obtain statistics, we scaled some of the laboratory parameters in a way that allowed us to make qualitative and quantitative predictions about the temporal-spectral properties of the signal with shorter run time. We verified the validity of this approach by comparing some runs with the unscaled simulations.

**Table 1. Parameters for Model and Laboratory OPOs**

Parameter	Dispersive OPO Model	Diffractive OPO Model	Laboratory OPOs: BBO/LiNbO <sub>3</sub>
$\lambda_p$	532 nm	532 nm	532/1064 nm
$\tau_p$	2 ns	10 ns	10 ns
$L_{\text{cavity}}$	20-mm ring	68-mm, 3-mirror ring	68–100-mm, 3-mirror ring
$L_{\text{crystal}}$	5 mm	7 mm	7–20 mm
$n_s (=n_p)$	1.654	1.654	1.654–2.193
$c/v_s$	1.67	Not applicable	1.67–2.26
$c/v_p$	1.70	Not applicable	1.70–2.25
$\beta_s$	$2.07 \times 10^{-25} \text{ s}^2/\text{m}$	Not applicable	$2.07\text{--}4.20 \times 10^{-26} \text{ s}^2/\text{m}$
$\beta_p$	$3.22 \times 10^{-25} \text{ s}^2/\text{m}$	Not applicable	$0.64\text{--}1.28 \times 10^{-25} \text{ s}^2/\text{m}$
$d_{\text{eff}}$	2.0 pm/V	2.0 pm/V	2.0–4.0 pm/V
$\rho$	Not applicable	56 mrad	56–35 mrad
Signal feedback	0.3	0.65	$\approx 0.65^a\text{--}0.65$
Pump diameter (FWHM)	Not applicable	0.65 mm	0.65–1.18 mm

<sup>a</sup>See Fig. 2.

We also simplified the diffractive model to eliminate the separate idler wave. This model was valuable in helping us understand transverse mode behavior. It accommodates the parameters of our laboratory OPOs, except, of course, their broad bandwidth. Table 1 summarizes the parameters used in the two simplified models.

The model that included both dispersion and diffraction used a simplification. The large bandwidth of the laboratory OPOs required a temporal resolution corresponding to several thousand sample points per round-trip time. Because of restrictions on run time and memory these requirements could not be handled in combination with the transverse dimensions. To simplify the problem we shortened the time slices in the model, effectively modeling only a small part of each round trip. Nevertheless, this model was sufficient to catch the essential features of the problem.

### 3. EXPERIMENTAL DESIGN

We used the setup diagrammed in Fig. 1 for our laboratory measurements. We studied two different OPOs to investigate crystals with both normal and anomalous dispersion. One OPO was pumped at 532 nm and used  $\beta\text{-BaB}_2\text{O}_4$  (BBO), which is normally dispersive at the signal wavelength of 1064 nm. The other was pumped at 1064 nm and used LiNbO<sub>3</sub>, which is anomalously dispersive at the signal wavelength of 2128 nm. Both OPOs used a three-mirror ring cavity pumped by 10-ns (FWHM) single-frequency pulses. The pump beams were spatially filtered to provide nearly Gaussian spatial profiles and were well collimated. The horizontal plane of the OPO cavity coincided with the crystal walk-off direction, so the pump and the signal polarizations were horizontal and vertical, respectively.

The 7-mm-long BBO crystal was cut at  $\theta = 23^\circ$ , and the BBO cavity length was 68 mm. We injection seeded the BBO OPO with a cw 1064-nm beam derived from the pump laser's injection-seeding laser so its phase was correlated with the 532-nm pump light. The seed beam was collimated and injected through the OPOs output coupler. The pump input coupler was coated for high transmission at 532 nm and high reflection at 1064 nm. The output

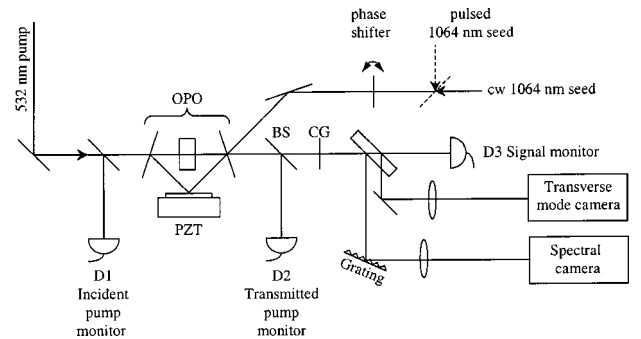


Fig. 1. Schematic diagram of the experimental apparatus for the BBO OPO: BS, beam splitter that reflects 532-nm light and transmits 1064-nm light; CG, colored glass filter that removes residual 532-nm light while transmitting 1064-nm light; OPO, degenerate OPO; PZT, piezoelectric transducer. The LiNbO<sub>3</sub> OPO experiment was similar, except no seed light was used.

coupler was coated for high transmission at 532 nm and 0.7 reflection at 1064 nm. The third mirror was a high reflector at 1064 nm and was mounted upon a piezoelectric transducer (PZT) for fine adjustment of the cavity length. We aligned the cavity mirrors interferometrically, using the 1064-nm seed beam. The pump beam was adjusted such that the seed and pump beams transmitted by the exit mirror were collinear. We oriented the BBO crystal for  $\Delta k = 0$  by adding pulsed 1064-nm light from the Nd:YAG pump laser to the cw seed light, adjusting the OPO cavity length to resonate the light, and rotating the BBO crystal to maximize the 532-nm light generated in the crystal. In all cases we were careful to remove all 1064-nm light from the pump beam to avoid unintentionally seeding the OPO.

The LiNbO<sub>3</sub> OPO was similar, except that the  $\theta = 45^\circ$  crystal was 20 mm long and the cavity length was 100 mm. We did not injection seed this OPO, and the  $\Delta k = 0$  angle for the crystal was not precisely determined. We interferometrically aligned the cavity using a He–Ne laser at 633 nm. The signal reflectivities of the three mirrors were similar to that of the BBO OPO with a round-trip feedback of  $\sim 0.65$ .

The ideal degenerate OPO cavity for our studies would have a constant round-trip reflectivity over a broad wave-

length range centered at the degenerate wavelength. For the BBO OPO the reflectivity should be flat from  $\sim 1000$  nm to  $\sim 1120$  nm to match the acceptance bandwidth of the BBO crystal. If the reflectivity over this range were to vary by a large amount the doubly resonant nature of the OPO would be compromised, and the doubly resonant OPO might behave more as a singly resonant device. The round-trip signal feedback of the actual BBO OPO is shown in Fig. 2. Feedback was 0.65 at degeneracy but had significant deviations over the target signal range, so when the spectrum covers  $\pm 50$  nm or more, the signal/idler symmetry is slightly broken. Nevertheless, we shall see that the qualitative behavior of the OPO is not seriously affected by this deviation from the ideal. Optical feedback for the LiNbO<sub>3</sub> OPO was more nearly uniform over the same range of  $\pm 400$  cm<sup>-1</sup> centered in this case on the 2128-nm wavelength. It varied from 0.7 at the blue end of the range to 0.4 at the red end.

The spatial profile of the 1064-nm signal beam from the BBO OPO was measured with a Cohu 4800 silicon array camera and a Big Sky beam profiling system. The 2128-nm beam from the LiNbO<sub>3</sub> OPO was measured with a Spiricon Pyrocam 1 pyroelectric array camera. We measured the far-field beam profiles by focusing the signal beam with a long-focal-length lens onto a camera located one focal length beyond the lens. The 1064-nm signal spectrum was measured with a 600-groove/mm grating that was oriented to diffract the light out of the plane of the OPO cavity. A 50-mm focal-length lens imaged the diffracted light onto the Cohu camera. The 2128-nm signal spectrum was measured similarly with the pyroelectric camera.

#### 4. PREDICTED SPECTRAL PROPERTIES

We begin our discussion of spectral properties by reporting the OPO's performance when the crystal is adjusted for exact phase-velocity matching of degenerate operation ( $\Delta k = 0$ ), and we look at the influence of cavity-length adjustments. With the OPO cavity length adjusted such that the round-trip phase of a degenerate signal wave is exactly  $m\pi$ , the unseeded signal spectrum is expected to be quite broad. The usual definition of acceptance bandwidth as the amount that the signal wave can tune before

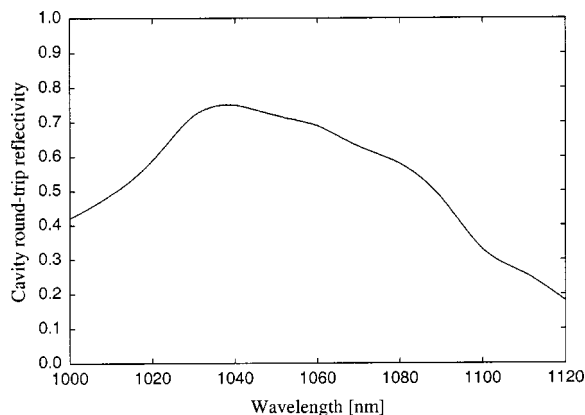


Fig. 2. Round-trip spectral reflectivity of the BBO OPO cavity mirrors near 1064 nm.

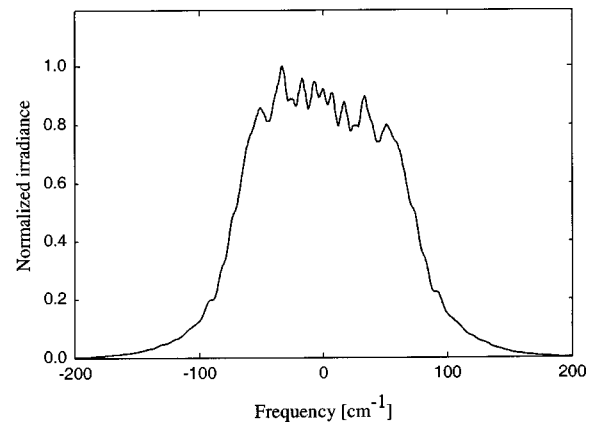


Fig. 3. Spectrum computed from the broadband, plane-wave OPO model for the parameters listed in Table 1, with the OPO cavity tuned to exact resonance ( $\delta = 0$ ). This is an average over 40 model runs, each with a different starting noise field. A simulated spectral resolution of  $5$  cm<sup>-1</sup> averages over the individual longitudinal modes.

the signal and the pump are dephased by  $2\pi$  owing to linear propagation during a single traverse of the crystal is

$$\Delta\omega_{\text{bw}} = \left( \frac{\pi}{L_{\text{crystal}}\beta_s} \right)^{1/2}. \quad (6)$$

Applying our dispersive model with the parameters listed in column 1 of Table 1 and with the BBO OPO pumped at twice threshold, we compute the spectrum shown in Fig. 3. This curve is the average of 40 model runs, each starting with a different simulation of the initial quantum noise. The computed spectrum actually consists of a series of spectrally distinct longitudinal cavity modes, but for display purposes we have applied a triangular weighting with a width of  $5$  cm<sup>-1</sup> to simulate the spectrum as it would appear if it were measured by a spectrometer with  $5$ -cm<sup>-1</sup> resolution. The calculated single-pass acceptance bandwidth in this case is  $\Delta\omega_{\text{bw}} = 293$  cm<sup>-1</sup>, whereas the linewidth (FWHM) computed by the simulation is  $140$  cm<sup>-1</sup>. This narrowing by a factor of 2 is consistent with the usual observation that nanosecond OPO linewidths are 2–4 times smaller than the crystal acceptance bandwidth.

When it is viewed in the time domain rather than in the spectral domain, we expect the signal to consist of a series of pulses of random length with phases alternating between the two maximum-gain values,  $\pi/4$  and  $-3\pi/4$ . The minimum duration of the pulses should be limited by the signal's group-velocity dispersion to approximately  $\sqrt{\pi\beta_s L_{\text{crystal}}}$ , which in this case is  $0.1$  ps. Typical computed time sequences are illustrated in Fig. 4. These are short-time slices early in the signal pulse (top) and late in the signal pulse (bottom). The phase, represented by the solid curves, alternates between the two expected values of  $\pi/4$  and  $-3\pi/4$ . The irradiance, represented by the dashed curves, is modulated, going to zero at the transitions between the constant-phase domains. Early in the signal pulse (top), the pulse widths and peak irradiances

vary more-or-less randomly, reflecting the random nature of the start-up noise, whereas late in the pulse (bottom) the irradiance values are somewhat stabilized at a level set by pump depletion. Note that the signal–pump walk-off time for a single pass of the crystal is 0.43 ps with the pump propagating slower than the signal, so the leading edges of the signal pulses are pumped by less-depleted pump light. The longer signal pulses have shapes that resemble damped oscillation with the highest irradiance at the leading edge of the pulse, followed by an equilibrium level that is lower by a factor of  $\sim 2$ . The damping time is comparable to the 0.43-ps walk-off time. The phase is fairly well confined to the two optimum values that are separated by  $\pi$ . The signal wave may be thought of as a wave with nearly constant phase but with an amplitude that is reversing sign at each irradiance null. This signal wave with nearly constant phase but strong amplitude modulation is in marked contrast to previous observations<sup>16</sup> that the signal wave from a singly resonant nanosecond OPO was nearly purely phase modulated, with little amplitude modulation.

Note that the calculated spectrum in Fig. 3 is slightly unbalanced between red and blue energy. Only a small fraction of this imbalance can be attributed to the difference between energy and photon number. This violation of the Manley–Rowe relation, which states that the red and the blue branches should have equal numbers of photons, can be explained by the fact that the group-velocity dispersion in this case tends to move red light to the lead-

ing edges of the signal pulses. Because the pump's group velocity is slower than that of the signal, the leading edges of the signal pulses are pumped by less-depleted pump light, preferentially amplifying the red light. Therefore, if the sign of the signal's group-velocity dispersion were reversed, or if the pump's group velocity were faster than that of the signal, the blue part of the signal spectrum would be stronger. We verified both effects using our model. Note also that the spectrum of Fig. 3 is somewhat flat-topped rather than Gaussian in profile, which can be explained in similar terms. Longer pulses in the signal-pulse train contribute predominantly to frequencies near the spectral center, but, as we have seen, these pulses suffer most from pump depletion. This result suggests that as the OPO is pumped further above threshold, the center of the signal spectrum should be progressively suppressed relative to the spectral wings, an effect that we also verified using our model.

The results just described were for the cavity length tuned to cause a signal wave to resonate exactly at frequency  $\omega_p/2$ . If the OPO cavity length is increased or decreased by a fraction of a signal wavelength, giving a round-trip phase of  $(m\pi \pm \delta)$ , the signal wave would accumulate an undesired phase of  $\pm\delta$  on each cavity round trip. Parametric gain could partially compensate by pulling the signal phase toward its optimum value, but the gain per pass would be reduced. However, if we assume that the signal splits into two frequency components ( $\omega_+ = \omega_0 + \Delta\omega$ ) and ( $\omega_- = \omega_0 - \Delta\omega$ ), the resultant shift in the quantity  $(\phi_+ + \phi_-)$  on each trip through the crystal might compensate for the phase,  $\delta$ , permitting gain and oscillation. The single-pass phase shift that is due to spectral splitting is

$$d(\phi_+ + \phi_-) = L_{\text{crystal}}(dk_+ + dk_-) \quad (7)$$

$$= L_{\text{crystal}} \left( \frac{dk_0}{d\omega} \Delta\omega + \frac{1}{2} \frac{d^2k_0}{d\omega^2} \Delta\omega^2 - \frac{dk_0}{d\omega} \Delta\omega + \frac{1}{2} \frac{d^2k_0}{d\omega^2} \Delta\omega^2 \right) \quad (8)$$

$$= L_{\text{crystal}} \frac{d^2k_0}{d\omega^2} \Delta\omega^2. \quad (9)$$

Using the definition of  $\beta$  given above, we can rewrite Eqs. (7)–(9) as

$$d(\phi_+ + \phi_-) = -2L_{\text{crystal}} \Delta\omega^2 \beta_s. \quad (10)$$

Assuming that the phase correction that is due to spectral splitting cancels that which is due to the cavity-length change gives

$$2\delta = -2L_{\text{crystal}} \Delta\omega^2 \beta_s. \quad (11)$$

Solving for  $\Delta\omega$  gives

$$\Delta\omega = \left( \frac{-\delta}{L_{\text{crystal}} \beta_s} \right)^{1/2}, \quad (12)$$

where  $\Delta\omega$  is half of the signal-wave spectral splitting necessary to compensate for the phase shift that is due to cavity detuning. Note that  $\Delta\omega$  is real only if  $\delta$  and  $\beta_s$

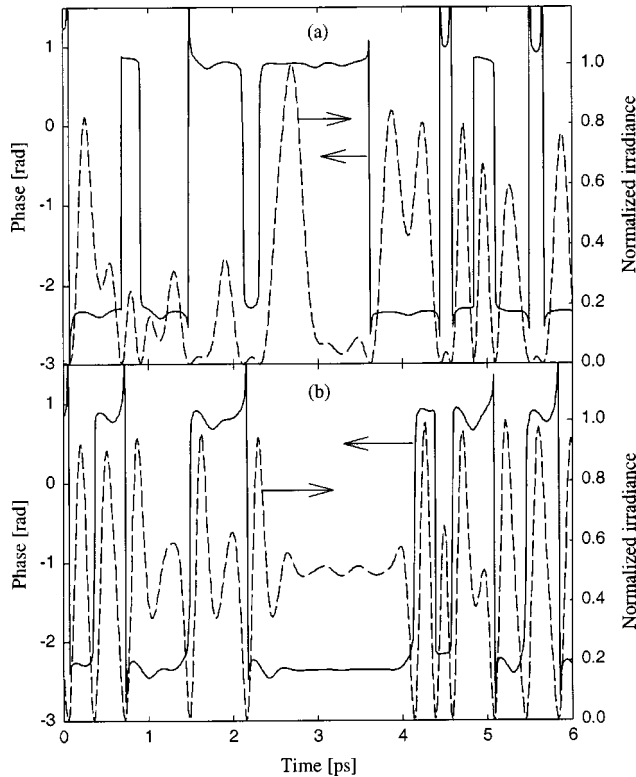


Fig. 4. Short-time slices of a signal wave calculated from the broadband, plane-wave OPO model for the parameters listed in Table 1, with the OPO cavity tuned to exact resonance ( $\delta = 0$ ) (a) early in the signal pulse and (b) late in the signal pulse. Solid curves, signal phases; dashed curves, normalized signal irradiances.

have opposite signs. For a crystal that is normally dispersive at the signal frequency, such as BBO at 1064 nm,  $\beta_s > 0$ , meaning that group velocity decreases with increasing frequency. In this case, only shortening the OPO cavity ( $\delta < 0$ ) results in spectral splitting. Lengthening the cavity does not. The situation is reversed if signal dispersion is anomalous, as it is for our LiNbO<sub>3</sub> OPO. In that case only lengthening the cavity will split the signal spectrum.

We verified these notions by using our numerical model of a normally dispersive OPO. Figure 5(a) shows a calculated signal spectrum for  $\delta = -0.1\pi$ . The splitting predicted by Eq. (12) is  $185 \text{ cm}^{-1}$ , in good agreement with the model-generated splitting of  $180 \text{ cm}^{-1}$ . If we lengthen rather than shorten the cavity, we obtain the spectrum shown in Fig. 5(b), which is narrower than the resonant-cavity spectrum. Our model verifies that reversing the sign of  $\beta_s$  reverses this behavior, so lengthening the cavity splits the spectrum whereas shortening it does not.

Bearing in mind that the phase shift that is due to linear propagation of the split spectrum is the same phase shift that sets the acceptance bandwidth, it is obvious that the spectral splitting should be comparable to the acceptance bandwidth. We can see this by comparing Eq. (6) with Eq. (12). The result implies that the crystal can always accommodate the predicted spectral splittings within its acceptance bandwidth, so they should be readily observed in any type I degenerate OPO with a

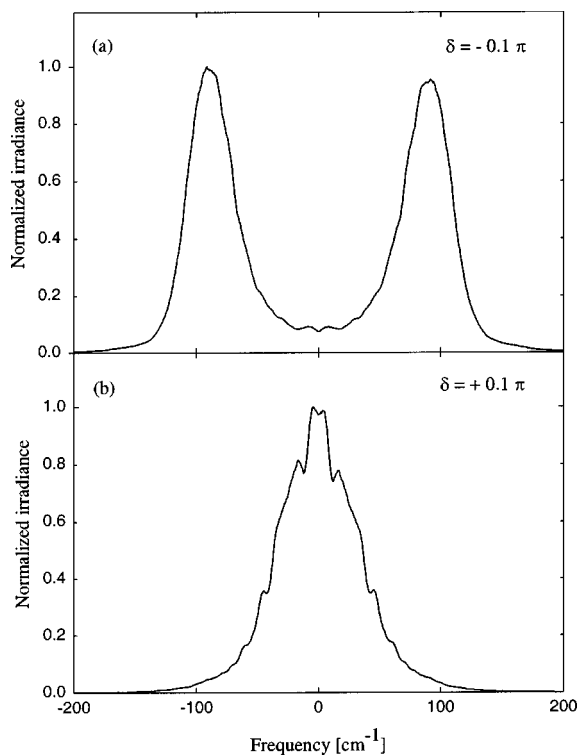


Fig. 5. Spectra computed from the broadband, plane-wave OPO model for parameters listed in Table 1 (a) with the OPO cavity shortened from resonance so  $\delta = -0.1\pi$  and (b) with the OPO cavity lengthened from resonance so  $\delta = +0.1\pi$ . These are averages over 40 model runs, each with a different starting noise field. A simulated spectral resolution of  $5 \text{ cm}^{-1}$  averages over the individual longitudinal modes.

cavity-length detuning of the proper sign—shortened for crystals that are normally dispersive at the signal wavelength or lengthened for anomalously dispersive crystals.

It is also possible and probably more insightful to analyze the splitting in time rather than in frequency. For a short pulse propagating through a crystal with normal group-velocity dispersion ( $\beta > 0$ ), the red component moves toward the front of the pulse while the blue component lags, giving the pulse a linear frequency chirp. Because frequency is the negative time derivative of phase in our notation, the phase must assume a parabolic time profile with the phase advanced at the center of the pulse and retarded in the wings. It is this phase advance in the pulse center that compensates for a shortened cavity. Because the phase advance depends on the pulse's duration, for a given cavity detuning there is a pulse length that optimally compensates for the change in cavity length at the pulse center. We can calculate the phase shift and the optimum pulse duration by using the linear propagation equation expressed in a frame moving at the group velocity of the signal pulse:

$$\frac{\partial \epsilon}{\partial z} = -i\beta_s \frac{\partial^2 \epsilon}{\partial t^2}. \quad (13)$$

Assuming that the pulses are those associated with amplitude modulating a degenerate carrier wave with the modulation factor  $\sin(\Delta\omega t)$ , corresponding to a spectral splitting of  $2\Delta\omega$ , we can calculate the modulation frequency that best compensates for cavity detuning. Differentiating the modulated signal envelope

$$\epsilon = \epsilon_0 \sin(\Delta\omega t) \quad (14)$$

gives

$$\frac{\partial^2 \epsilon}{\partial t^2} = -\Delta\omega^2 \epsilon, \quad (15)$$

so the field evolution at the pulse center obeys

$$\frac{\partial \epsilon}{\partial z} = i\beta_s \Delta\omega^2 \epsilon. \quad (16)$$

Thus the single-pass phase shift at the pulse center is

$$\phi = L_{\text{crystal}} \beta_s \Delta\omega^2. \quad (17)$$

Equating this phase shift with the negative of cavity detuning  $\delta$  gives

$$\Delta\omega = \left( \frac{-\delta}{L_{\text{crystal}} \beta_s} \right)^{1/2}, \quad (18)$$

in agreement with our previous expression for the spectral splitting. In the language of stability studies<sup>1-4</sup> this is a modulational instability that favors growth of amplitude modulations with the favored periodicity. If the signal is initiated by random noise, pulses of this duration will experience the greatest gain, so the signal wave will eventually consist of a series of fairly regularly spaced pulses with phases alternating between  $\pi/4$  and  $-3\pi/4$ . This is vividly illustrated by the time histories shown in Fig. 6 computed for  $\delta = -0.1\pi$ . As the signal wave

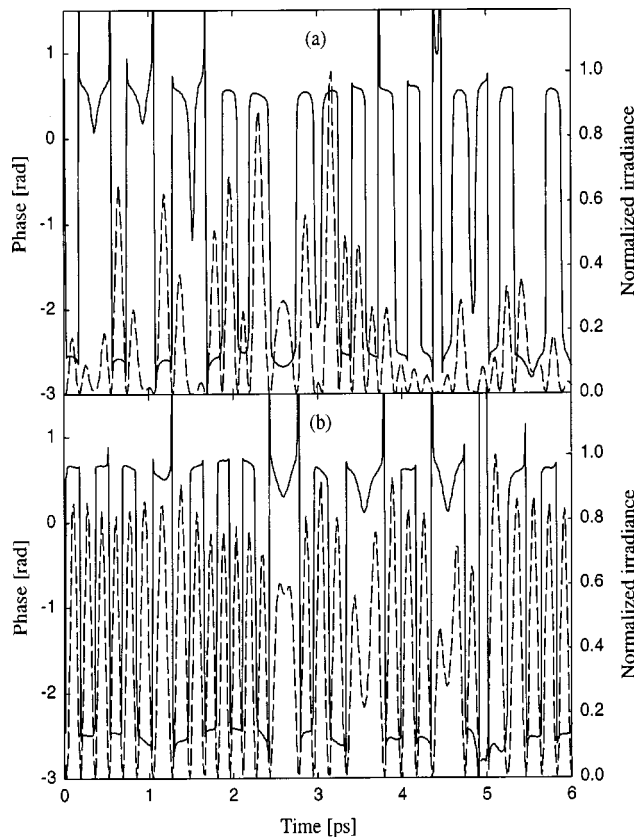


Fig. 6. Short-time slice of a signal wave calculated from the broadband, plane-wave OPO model for parameters listed in Table 1 with the OPO cavity shortened such that  $\delta = -0.1\pi$ : (a) early in the signal pulse, (b) late in the signal pulse. Solid curves, signal phases; dashed curves, normalized signal irradiances.

evolves, the pulse trains tend to become more regular, with the favored modulation period becoming dominant.

## 5. PREDICTED TRANSVERSE MODE PROPERTIES

The signal wave can also acquire a phase shift if a small tilt rather than a spectral split is assumed. As is well known, in a Fabry–Perot cavity a tilt angle of  $\theta$  reduces the signal wave's round-trip phase by

$$\phi_{\text{tilt}} = -\frac{\theta^2}{2} k_s (L_{\text{crystal}}/n_s + L_{\text{cavity}} - L_{\text{crystal}}). \quad (19)$$

Setting this tilt-induced phase to compensate for the cavity-detuning-induced phase, we get

$$\theta = \{2\delta/k_s [L_{\text{cavity}} + L_{\text{crystal}}(n_s^{-1} - 1)]\}^{1/2}. \quad (20)$$

Only  $\delta > 0$  is allowed in this expression, implying that only cavities slightly longer than resonant can favor tilted beams. This is in contrast to spectral splitting, which can be induced by either shortened or lengthened cavities depending on whether dispersion is normal or anomalous, respectively. Consequently, for normally dispersive crystals we expect shortened cavities to generate a split spectrum and lengthened cavities to produce tilted beams. For anomalously dispersive crystals, shortened cavities

cannot be compensated for by either beam tilts or spectral splitting, so they will probably have high thresholds. Lengthened cavities can be compensated for by either beam tilt or spectral splitting or by both with a coupling between tilts and splittings.<sup>11</sup>

Restricting the discussion for the moment to normally dispersive crystals, if we have radial symmetry for the pump beam and the cavity we might expect the lengthened cavities to create a ring-shaped signal wave in the far field, with a ring angle of  $\theta$ . In the near field, such a conical beam would create a radial interference pattern with rings of alternating phase separated by nulls. These rings would cause the diffraction term in Eq. (1) to produce phase shifts in analogy with those produced by the group-velocity dispersion term discussed in connection with spectral splitting. This is an example of spatial modulational instability and near-field spatial pattern formation. Such spatial pattern formation has been experimentally demonstrated in other types of nonlinear oscillators.<sup>1-4</sup>

Using the OPO parameters listed in column 2 of Table 1 yields for the far-field ring angle, according to Eq. (20), 2 mrad for a cavity detuning of ( $\delta = \pi/4$ ). Figure 7 shows the corresponding model-generated far-field signal fluence pattern at a phase shift of  $\delta = \pi/4$ . As the figure shows, the computed far-field ring angle is near the predicted 2 mrad. Figure 8 shows the corresponding computed phase and irradiance profiles at the crystal exit face at a time midway through the signal pulse. This is a vertically centered, horizontal (critical plane) slice through the signal beam. The pattern is similar to the time patterns, with domains of nearly constant phase separated by near zeros of irradiance. The pattern is not so distinctly defined as the time patterns because of the relatively strong role of diffraction for our small beam diameter. Although we do not show a plot of the results, we found that, as the beam diameter was increased, the pattern became more clearly defined, with more nearly constant phase across each zone and with deeper irradiance minima at the zone boundaries.

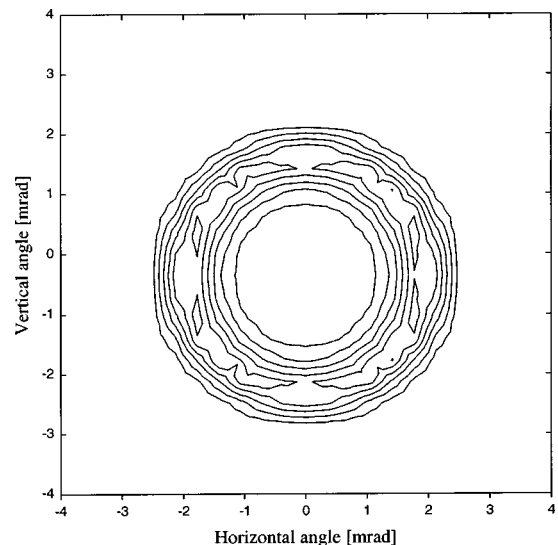


Fig. 7. Far-field signal fluence profile computed from the diffractive, monochromatic OPO model for  $\delta = 0.25\pi$ .

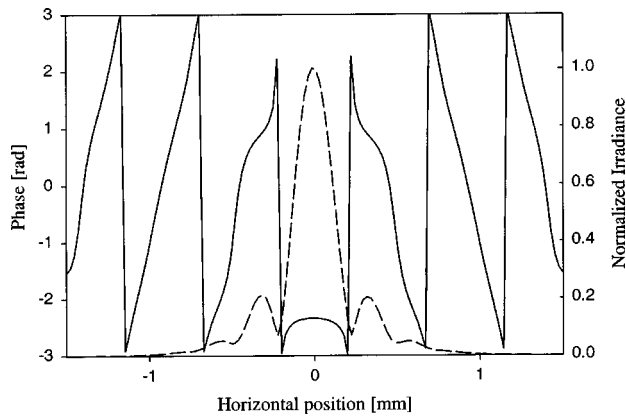


Fig. 8. Vertically centered horizontal (critical plane) slice of the computed signal irradiance (dashed curve) and phase (solid curve) at the crystal's exit face at the peak of the signal pulse.

## 6. MEASURED SPECTRA AND TRANSVERSE MODES

### A. $\beta$ -BaB<sub>2</sub>O<sub>4</sub> OPO

In Fig. 9 we summarize the measured signal spectra and far-field patterns of the unseeded, 532-nm pumped OPO for  $\Delta k = 0$ , with cavity detunings of  $\delta \approx -0.15\pi$  (top pair),  $\delta \approx 0.0\pi$  (middle pair), and  $\delta \approx 0.25\pi$  (bottom pair). For a shortened cavity the spectrum splits as discussed above, with a splitting in agreement with Eq. (12) to within our experimental uncertainties in frequency calibration and cavity-length control. The strong asymmetry between the red and blue spectral branches is due almost entirely to the detector's spectral response, which falls in sensitivity by approximately a factor of 10 from left to right over the wavelength range plotted. The OPO cavity mirrors also vary in reflectivity over this range but in such a way that they tend to counter the variation in detector response. The far-field pattern for the shortened cavity indicates that the beam quality is high. There is some asymmetry in the out-of-plane direction, possibly because of a slight misalignment of the pump beam or the cavity mirrors. For the resonant cavity (middle row of Fig. 9) the beam quality remains good but the spectrum has coalesced to a single peak with a slight dip at line center. The measured linewidth of  $490 \text{ cm}^{-1}$  is  $\sim 60\%$  of the calculated single-pass acceptance bandwidth of Eq. (6), a narrowing factor that is not too different from the 50% for the case modeled above. The dip at line center is consistent with simulations for an OPO pumped at four times threshold to approximate our experimental conditions. When the cavity is lengthened by approximately an eighth of a wavelength (bottom row of Fig. 9) the spectrum narrows, and the far-field pattern becomes ringlike, as expected. The contour plots show a ring pattern that is strongest in the vertical directions, in contrast to the model prediction of slightly stronger signal in the horizontal directions. We have no definitive explanation for this discrepancy, but we suspect a small misalignment of the cavity mirrors or the pump beam.

Figure 10 shows how the measured OPO signal energy varied as the cavity length was swept through 1.5 wavelengths. The points of highest energy correspond to  $\delta = m\pi$ , while the hashed zones correspond to either ring-

mode or split-spectrum operation. The conversion efficiency is equal whether  $m$  is odd or even but falls progressively as the cavity is tuned away from the resonant points.

### B. LiNbO<sub>3</sub> OPO

Figure 11 shows the corresponding plot of signal energy as the cavity length of the LiNbO<sub>3</sub> OPO is changed. In this case the curves are more asymmetric because a cavity shortened slightly from resonance supports neither a split spectrum nor a ring mode, whereas a cavity lengthened slightly supports both. In the zones labeled I in Fig. 11 the mode is a ring and the spectrum is split, whereas

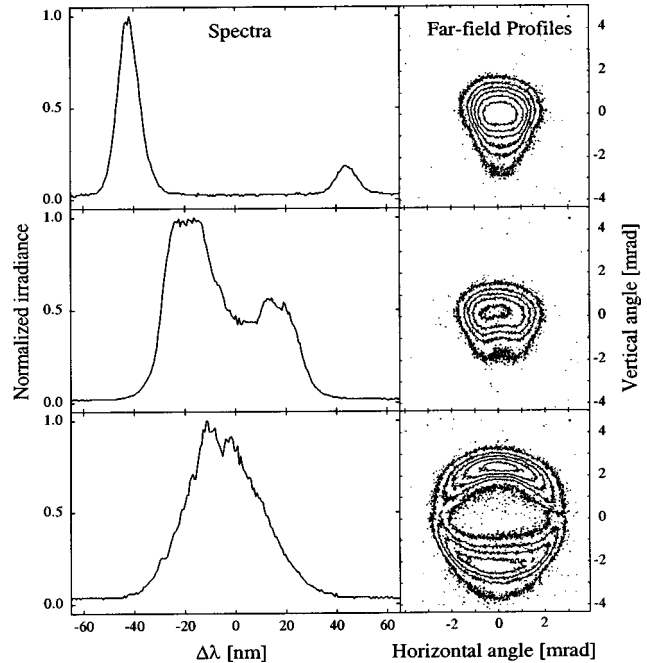


Fig. 9. Left, measured BBO OPO unseeded signal spectra and right, far-field beam profiles for cavity detunings of  $\delta \approx -0.15\pi$  (top row),  $\delta \approx 0.0\pi$  (middle row), and  $\delta \approx 0.25\pi$  (bottom row).

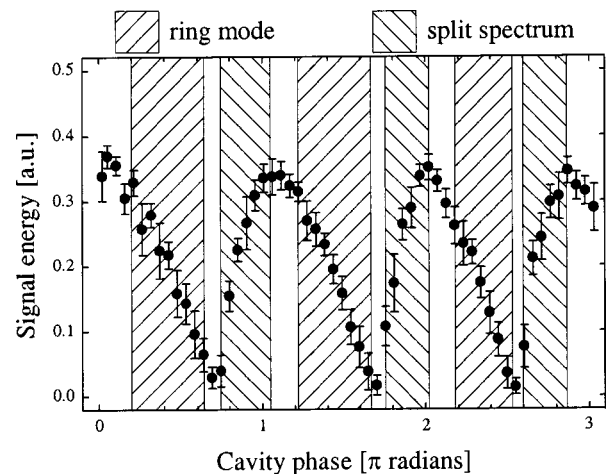


Fig. 10. Measured BBO OPO unseeded-signal energy as the length of the OPO cavity is scanned over 1.5 signal wavelengths. The error bars represent the experimental pulse-to-pulse variation in signal energy. Split spectra and ring modes are individually present in the separate zones indicated by hatching.

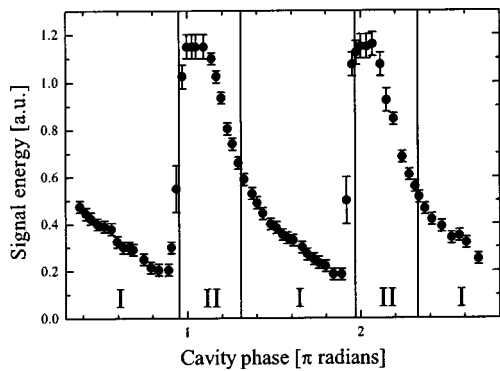


Fig. 11. Measured LiNbO<sub>3</sub> OPO unseeded-signal energy as the length of the OPO cavity is scanned over 1.5 signal wavelengths. The error bars represent the experimental pulse-to-pulse variation in signal energy. In the zones labeled I the spectrum is split and the far-field transverse mode is a ring. In the zones labeled II spectral splitting and ring modes are not evident within the available spectral and spatial resolution of the experiment.

in the zones labeled II the mode is filled and the spectrum is a single peak. This behavior is in accord with the predictions of the models discussed above.

## 7. INJECTION SEEDING

Because of the phase sensitivity of parametric amplification, we included a phase-adjusting plate in the 1064-nm seed beam for the BBO OPO to provide adjustment of the signal phase relative to the pump phase. This adjustment does not affect the seed frequency, so it does not alter the strength of the seed light circulating in the unpumped cavity. Note that if the cavity is tuned such that  $m$  is an even integer, the seed will resonate, but if  $m$  is an odd integer the cavity will be antiresonant for the seed light. We found in simulations of the former that if the seed phase is not one of the optimal phases,  $\pi/4$  or  $-3\pi/4$ , relative to the pump, parametric gain quickly pulls the phase of the circulating seed light to the nearer of the optimal phases. Only when the seed phase is within 0.01 rad of the most unfavorable phases of  $-\pi/4$  or  $3\pi/4$  does seeding fail. Seeding also fails in the antiresonant case because there is little seed light circulating in the cavity. Experimentally, we found that, for  $m$  even, seeding is successful for all seed phases. This is consistent with our model result if we acknowledge that cavity and seed alignments are imperfect so that in practice we are unlikely to control the phase over the entire beam diameter to within 0.01 rad as our model required for seeding failure. Because seeding is always successful for  $m$  even, it is necessary to suppress residual 1064-nm light in the 532-nm pump light to a single photon or less per pulse to avoid inadvertent seeding. We find experimentally that seeding always fails for  $m$  odd.

When the BBO OPO cavity was shortened ( $\delta < 0$ ) such that the free-running spectrum split, seeding was unsuccessful in both model and experiment. The far-field pattern revealed a high-quality beam just as in the corresponding case with no seed. When the cavity was tuned to  $\delta = 0$ , the OPO seeded as described above and the beam quality was good. When the cavity was lengthened further ( $\delta > 0$ ), seeding was successful over the range

that would produce a ring mode in the unseeded OPO. It still had a ringlike far-field pattern, but the frequency was narrowed to a single longitudinal cavity mode of the OPO. To summarize the seeding behavior of the BBO OPO: Starting at  $\delta = 0$ ,  $m$  even, seeding was successful and, as the cavity was lengthened, the laser seeded over the region of the ring mode, followed by failure to seed as the spectrum split. Then the laser passed through the  $\delta = 0$ ,  $m$  odd point until the ring mode reappeared and again seeded, followed by seeding failure as the spectrum again split, followed by successful seeding as the cycle was completed at  $\delta = 0$ ,  $m$  even.

## 8. BROADBAND PUMPING

Figure 12 shows signal energy versus pump energy for the BBO OPO when the pump laser was unseeded. The threshold was 3–4 times higher than for the seeded pump. This is not surprising if we consider the phase-sensitive nature of parametric gain. The unseeded pump laser has a bandwidth of  $\sim 0.3 \text{ cm}^{-1}$ , implying a pump coherence length less than 3 cm, or approximately one half of the OPO's round-trip length. The circulating signal sees an essentially random pump phase on each cavity pass, and, because its phase cannot be pulled significantly by parametric gain on a single crystal pass, its average gain is substantially reduced relative to its value for a single-frequency pump.

## 9. CONCLUSIONS

We have shown that, for a crystal tuned for  $\Delta k = 0$  at degeneracy in a type I OPO, a round-trip signal phase of  $m\pi$ , where  $m$  is an integer, gives a single spectral peak centered at the degenerate wavelength and an untilted far-field spatial pattern. If the round-trip phase is slightly less than  $m\pi$ , that is, if the cavity is slightly shortened, the spatial pattern remains untilted but the spectrum splits if the crystal's group-velocity dispersion is normal ( $\beta_s > 0$ ) or narrows if it is anomalous ( $\beta_s < 0$ ). If the cavity is lengthened and the crystal is normally dis-

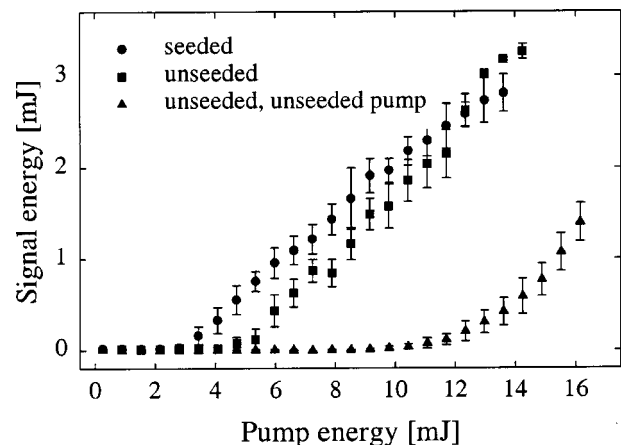


Fig. 12. Measured signal energy versus pump energy for seeded and unseeded BBO OPOs pumped by a seeded Nd:YAG laser and for an unseeded BBO OPO pumped by an unseeded Nd:YAG laser. The cavity is tuned to  $\delta = 0$  when the pump laser is injection seeded.

persive, the far-field pattern is ring shaped, with a radius given by Eq. (20). If the crystal is anomalously dispersive, both beam tilt and spectral splitting are favored in this situation. A coupling of the two effects is predicted by our model that includes both broad bandwidth and diffraction. Larger ring angles are associated with smaller spectral splitting, and smaller ring angles are associated with larger spectral splitting. Unfortunately, we were unable to verify this effect experimentally because of the limitations of our laboratory equipment.

For the normally dispersive OPO that we studied we found that, when  $m$  is an even integer or when the far field is a ring, injection seeding the OPO is effective, regardless of the phase of the seed light relative to the pump phase. Seeding fails if  $m$  is an odd integer and also when the spectrum is split as a result of cavity detuning. We also found that pumping the BBO OPO with a multilongitudinal-mode pump laser is ineffective because the signal phase cannot track the pump phase to maintain optimal signal parametric gain. The result is a pump threshold substantially higher and a conversion efficiency substantially lower than for a single-mode pump.

The sensitivity of the signal's transverse mode and spectrum demonstrated here indicates that stable OPO performance of a degenerate type I OPO requires a cavity-length stability of approximately one hundredth of a signal wavelength. This stability requirement is not unusual among doubly resonant OPOs, but what is unique about type I degenerate OPOs is the large wavelength splitting that is induced by cavity-length detuning and the fact that normally dispersive crystals cannot accommodate cavity lengthening with spectral adjustment and instead exhibit distorted transverse profiles, whereas anomalously dispersive crystals cannot accommodate cavity shortening with either spectral splitting or distorted transverse profiles. We have discussed specifically OPOs based on negative uniaxial crystals for which the pump and signal polarizations are extraordinary and ordinary, respectively. Positive uniaxial crystals have reversed polarizations, but this should have little influence on the behavior discussed above.

We presented modeling results and measurements for the case of  $\Delta k = 0$ . In nondegenerate OPOs the value of  $\Delta k = 0$  is often of overriding significance, largely determining the spectral characteristics of the signal wave. Such is not the case for type I degenerate OPOs, for which the detuning of the cavity length is much more important than the value of  $\Delta k = 0$ . We observed that when the cavity-length detuning causes the spectrum to split we can slightly improve the conversion efficiency of the OPO by adjusting  $\Delta k$  to equal zero for the split spectrum rather than for the truly degenerate operation. However, such an adjustment of  $\Delta k$  has little influence on the spectrum. The performance of the OPO is dominated by the cavity-length detuning rather than by  $\Delta k$  in all cases when  $\Delta k$  is small at degeneracy.

## ACKNOWLEDGMENTS

We acknowledge the assistance of C. K. Schultz in running several numerical simulations. Sandia National Laboratory is a multiprogram laboratory operated by Sandia Corporation, a Lockheed Martin Company, for the U.S. Department of Energy's National Nuclear Security Administration under contract DE-AC04-94AL8500.

## REFERENCES

1. S. Longhi, "Hydrodynamic equation model for degenerate optical parametric oscillators," *J. Mod. Opt.* **43**, 1089–1094 (1996).
2. G.-L. Oppo, M. Brambilla, and L. A. Lugiato, "Formation and evolution of roll patterns in optical parametric oscillators," *Phys. Rev. A* **49**, 2028–2032 (1994).
3. M. Santagiustina, P. Colet, M. San Miguel, and D. Walgraef, "Walk-off and pattern selection in optical parametric oscillators," *Opt. Lett.* **23**, 1167–1169 (1998).
4. M. Santagiustina, P. Colet, M. San Miguel, and D. Walgraef, "Space inversion symmetry breaking and pattern selection in nonlinear optics," *J. Opt. B* **1**, 191–197 (1999).
5. L. I. Plimak and D. F. Walls, "Dynamical restrictions to squeezing in a degenerate optical parametric oscillator," *Phys. Rev. A* **50**, 2627–2641 (1994).
6. S. Prasad, "Quantum-noise and squeezing in an optical parametric oscillator with arbitrary output-mirror coupling. 3. Effect of pump amplitude and phase fluctuations," *Phys. Rev. A* **49**, 1406–1426 (1994).
7. H. Deng, D. Erenso, R. Vyas, and S. Singh, "Entanglement, interference, and measurement in a degenerate parametric oscillator," *Phys. Rev. Lett.* **86**, 2770–2773 (2001).
8. S. Chaturvedi, K. Dechoum, and P. D. Drummond, "Limits to squeezing in the degenerate optical parametric oscillator," *Phys. Rev. A* **65**, 033805 (2002).
9. R. C. Eckardt, C. D. Nabors, W. J. Kozlovsky, and R. L. Byer, "Optical parametric oscillator frequency tuning and control," *J. Opt. Soc. Am. B* **8**, 646–667 (1991).
10. A. J. Henderson, M. J. Padgett, F. G. Colville, J. Zhang, and M. H. Dunn, "Doubly-resonant optical parametric oscillators: tuning behaviour and stability requirements," *Opt. Commun.* **119**, 256–264 (1995).
11. K. Staliunas, "Three-dimensional structures and spatial solitons in optical parametric oscillators," *Phys. Rev. Lett.* **81**, 81–84 (1998).
12. W. J. Alford, R. J. Gehr, R. L. Schmitt, A. V. Smith, and G. Arisholm, "Beam tilt and angular dispersion in broad-bandwidth nanosecond optical parametric oscillators," *J. Opt. Soc. Am. B* **16**, 1525–1532 (1999).
13. G. Arisholm, "Quantum noise initiation and macroscopic fluctuations in optical parametric oscillators," *J. Opt. Soc. Am. B* **16**, 117–127 (1999).
14. A. V. Smith, R. J. Gehr, and M. S. Bowers, "Numerical models of broad-bandwidth nanosecond optical parametric oscillators," *J. Opt. Soc. Am. B* **16**, 609–619 (1999).
15. A. V. Smith, W. J. Alford, T. D. Raymond, and M. S. Bowers, "Comparison of a numerical model with measured performance of a seeded, nanosecond KTP optical parametric oscillator," *J. Opt. Soc. Am. B* **12**, 2253–2267 (1995).
16. D. J. Armstrong and A. V. Smith, "Tendency of nanosecond optical parametric oscillators to produce purely phase-modulated light," *Opt. Lett.* **21**, 1634–1636 (1996).